Scientific Research Publishing

World Journal of Condensed Matter Physics, 2026, 16(4), 138-160
https://www.scirp.org/journal/wjcmp
ISSN Online: 2160-6927
ISSN Print: 2160-6919

Size- and Shape-Dependent Thermophysical and Thermoelastic Properties of High-Entropy Alloy CoCrFeMnNi Nanostructures

Pinky Kumari, Sonal Swaraj, Mritunjay Kumar, Krishna Kumar, Nirjar Vrind*, Jagdhar Mandal

Department of Physics, Tilka Manjhi Bhagalpur University, Bhagalpur, India
Email: pinky123jmt@gmail.com; sonalswaraj91@gmail.com; mritunjaykr8272@gmail.com; kumarkrishna1401@gmail.com; *nirjarvrind9931@gmail.com; jmandal1284@gmail.com

How to cite this paper: Kumari, P., Swaraj, S., Kumar, M., Kumar, K., Vrind, N. and Mandal, J. (2026) Size- and Shape-Dependent Thermophysical and Thermoelastic Properties of High-Entropy Alloy CoCrFeMnNi Nanostructures. *World Journal of Condensed Matter Physics*, **16**, 138-160.
https://doi.org/10.4236/wjcmp.2026.164008

Received: August 28, 2026
Accepted: November 17, 2026
Published: November 20, 2026

Copyright © 2026 by author(s) and Scientific Research Publishing Inc.
This work is licensed under the Creative Commons Attribution International License (CC BY 4.0).
http://creativecommons.org/licenses/by/4.0/

Open Access

Abstract

High-entropy alloys (HEAs) represent a new generation of advanced materials with unique combinations of structural, mechanical and thermophysical properties. Among them, the equiatomic CoCrFeMnNi alloy, commonly known as the Cantor alloy, has attracted considerable attention because of its excellent mechanical strength, thermal stability, corrosion resistance and single-phase face-centered cubic (FCC) structure. In the present study, a theoretical approach is employed to investigate the size- and shape-dependent thermophysical and thermoelastic properties of CoCrFeMnNi HEA nanostructures. Six different morphologies, namely spherical, tetrahedral, hexahedral, octahedral, nanowire and nanofilm structures, are considered over a size range of 5 - 55 nm at room temperature. The effects of particle size and morphology on cohesive energy, Helmholtz free energy, melting entropy, specific heat capacity, thermal expansion coefficient and bulk modulus are systematically investigated. The results demonstrate that these properties exhibit pronounced size and shape dependence at smaller dimensions because of the increasing contribution of surface atoms and reduced atomic coordination. With increasing particle size, the calculated properties gradually approach their corresponding bulk values as the surface contribution decreases. Among the investigated morphologies, tetrahedral nanostructures exhibit the strongest size-dependent behaviour, whereas nanofilms show the highest cohesive energy and Helmholtz free energy over the investigated size range. The differences among the various morphologies become progressively smaller with increasing particle size, indicating a transition from surface-dominated nanoscale behaviour to bulk-like thermodynamic and thermoelastic properties. These results demonstrate that particle size and morphology can serve as effective parameters for tailoring the thermophysical and thermoelastic behaviour of

CoCrFeMnNi HEA nanostructures.

Keywords

High-Entropy Alloy, Cantor Alloy, CoCrFeMnNi, Cohesive Energy, Specific Heat Capacity, FCC, Corrosion Resistance, Reliable Structure, Etc

1. Introduction

The discovery of high-entropy alloys (HEAs) has significantly expanded the field of alloy development by introducing a class of materials composed of multiple principal elements, generally present in near-equiatomic or concentrated proportions. Unlike conventional alloys, which typically contain one or two principal elements, HEAs derive their distinctive characteristics from the complex interactions among their constituent elements and the associated configurational entropy. The concept of HEAs was initially proposed for alloys containing five or more principal elements, with each constituent generally present in the range of 5 - 35 at.% [1]. The high configurational entropy associated with these multicomponent systems was initially considered to favour the formation of simple solid-solution phases over complex intermetallic compounds [2] [3]. However, subsequent experimental investigations have demonstrated that the phase stability of HEAs is governed by a complex interplay among entropy, enthalpy, atomic size mismatch and other thermodynamic and kinetic factors. Consequently, HEAs may exhibit single-phase as well as multiphase microstructures [2]-[8].

Among the various HEA systems, the equiatomic CoCrFeMnNi alloy, commonly referred to as the Cantor alloy, has received considerable scientific attention because of its predominantly single-phase face-centered cubic (FCC) structure and excellent combination of mechanical and physical properties [2] [3] [9]-[15]. The alloy exhibits high strength, good ductility, excellent damage tolerance and considerable structural stability over a wide range of temperatures. Its remarkable mechanical response, particularly at low temperatures, makes it an attractive candidate for applications involving demanding thermal and mechanical environments [16]. Furthermore, the multicomponent nature of CoCrFeMnNi provides opportunities for tailoring its physical properties through changes in composition, microstructure and structural dimensions [17].

The thermophysical properties of HEAs, including thermal conductivity, specific heat capacity, thermal diffusivity, coefficient of thermal expansion and electrical resistivity play important roles in determining their response under different thermal and operating conditions [18] [19]. A detailed understanding of these properties is essential for assessing the suitability of HEAs in applications such as energy conversion, catalysis, aerospace systems, nuclear technologies, cryogenic engineering and high-temperature structural components. Previous experimental and theoretical studies have demonstrated that the thermophysical properties of

concentrated solid-solution alloys are strongly influenced by chemical complexity and elemental composition. In particular, the constituent elements can significantly modify thermal transport and related physical properties [20]-[22].

Recent developments in nanotechnology have enabled the fabrication and investigation of HEA-based nanostructures, including nanoparticles, nanowires, thin films and nanocrystalline materials [23]. When the characteristic dimensions of a material are reduced to the nanoscale, the surface-to-volume ratio increases substantially and a significant fraction of atoms are located at or near the surface. These surface atoms possess reduced coordination numbers and consequently different bonding environments from those of atoms in the interior. As a result, properties that are relatively stable in bulk materials can exhibit pronounced size and morphology dependence at the nanoscale. Surface energy, atomic coordination, lattice vibrations and structural relaxation can therefore influence cohesive energy, thermodynamic response, thermal expansion, elastic properties and phase-transition behaviour [24]-[32].

Theoretical modelling provides an effective approach for investigating these size- and shape-dependent effects, particularly when systematic experimental data for different nanoscale morphologies are limited. The Debye model can be used to describe the vibrational contribution to thermodynamic properties, while surface-atom-based approaches provide a means of incorporating nanoscale size effects. In combination with suitable equations of state and size- and shape-dependent models, these approaches can be used to investigate the thermodynamic and thermoelastic behaviour of nanostructured materials [24]-[32].

Although considerable research has been conducted on the bulk thermophysical and mechanical properties of CoCrFeMnNi HEA, the systematic theoretical investigation of the combined effects of particle size and morphology on multiple thermophysical and thermoelastic properties of CoCrFeMnNi nanostructures remains an important area of study. In particular, a comparative analysis involving different geometries within a common theoretical framework can provide insight into the role of surface-atom fraction and morphology in determining nanoscale behaviour. Such an approach is useful for identifying how different nanostructure geometries deviate from bulk behaviour and how these deviations diminish with increasing characteristic size [33] [34].

Therefore, the present study focuses on the theoretical investigation of the size- and shape-dependent thermophysical and thermoelastic properties of CoCrFeMnNi HEA nanostructures. Six different geometries—spherical, tetrahedral, hexahedral, octahedral, nanowire and nanofilm—are considered over the size range of 5 - 55 nm at room temperature. The effects of size and morphology on cohesive energy, Helmholtz free energy, melting entropy, specific heat capacity, thermal expansion coefficient and bulk modulus are systematically evaluated using established size- and shape-dependent theoretical models. The objective is to elucidate the relationship between surface-atom fraction, morphology and the resulting thermodynamic and thermoelastic response and to determine the size range over which the

properties of the nanostructures gradually approach their corresponding bulk behaviour [35].

Although the thermophysical and mechanical properties of bulk and nanoscale CoCrFeMnNi high-entropy alloys have been widely investigated, a systematic understanding of the coupled effects of particle size and morphology on multiple thermophysical and thermoelastic properties within a common theoretical framework remains limited. The present work addresses this gap by establishing a unified theoretical analysis of six distinct CoCrFeMnNi nanostructures, namely spherical, tetrahedral, hexahedral, octahedral, nanowire and nanofilm geometries, over a wide size range of 5 - 55 nm.

The key novelty lies not merely in comparing different morphologies, but in systematically linking morphology-dependent surface-atom fraction and particle size with a broad set of interrelated thermophysical and thermoelastic properties, including cohesive energy, Helmholtz free energy, melting entropy, specific heat capacity, thermal expansion coefficient and bulk modulus. By employing a common size- and shape-dependent theoretical framework, the study reveals how variations in atomic coordination and surface contribution govern the morphology-dependent response of CoCrFeMnNi nanostructures.

A further novel aspect is the identification of a systematic transition from surface-dominated nanoscale behaviour to bulk-like behaviour with increasing particle size. The comparative analysis demonstrates that the differences among morphologies are most pronounced at small dimensions and progressively diminish as the characteristic size increases. In particular, tetrahedral nanostructures exhibit the strongest size sensitivity, whereas more compact geometries and nanofilms show comparatively weaker morphology-dependent variations for several properties [36].

2. Theoretical Formalism

The nanostructures are treated as chemically disordered, equiatomic single-component effective nanosolids. This approximation represents the five-element random solid solution through composition-averaged bulk inputs and a morphology-dependent surface-atom fraction. Individual Co/Cr/Fe/Mn/Ni local chemical environments, short-range chemical ordering, element-specific surface segregation, vacancies and atom-by-atom surface reconstruction are not explicitly resolved. Structural relaxation is therefore represented implicitly through the reduced-coordination/surface contribution of the adopted phenomenological models [37] [38]. These assumptions define the scope of the present analytical treatment and should not be interpreted as an atomistic prediction of segregation or local relaxation [39].

Geometry convention: D denotes the characteristic diameter of the spherical and hexahedral nanostructures. For octahedral and tetrahedral particles, a denotes the characteristic edge length used in the surface-atom expressions. For nanowires, l denotes the wire length and d is the atomic diameter; l is the nanowire

Table 1. Bulk numerical inputs used in the calculations.

Parameter	Value used/convention	Unit	Source/averaging method
Composition	$Co_{0.20}Cr_{0.20}Fe_{0.20}Mn_{0.20}Ni_{0.20}$	at. fraction	Equiatomic Cantor alloy; [2,3]
Atomic diameter, d	0.254	nm	Derived from a = 0.359 nm for FCC CoCrFeMnNi; $d = a/\sqrt{2}$ [33]
Bulk cohesive energy	≈386.7	kJ mol^{-1}	Magnitude of the reported 300 K cohesive energy, 4.009 eV atom^{-1}, converted using 1 eV atom^{-1} = 96.485 kJ mol^{-1} [33]
Bulk melting temperature, T_{mb}	1607	K	Experimental melting temperature of equiatomic CoCrFeMnNi reported by Vaidya *et al.* [34]
Bulk melting entropy, S_{mb}	≈8.3	J mol^{-1} K^{-1}	Derived from Equation (10) using the adopted bulk vibrational relation; Kumar *et al.* [28] and Ubbelohde [29]
Bulk heat capacity, C_{pb}	≈27.7	J mol^{-1} K^{-1}	494 J kg^{-1} K^{-1} at 25˚C converted using M = 0.056081 Kg mol^{-1}; [35]
Volumetric thermal expansion, ξ_b	45 × 10−6	K^{-1}	From $\alpha_L \approx 15 \times 10{-}6$ K^{-1} for CoCrFeMnNi; $\xi_b \approx 3\alpha_L$; Laplanche *et al.* [1]
Bulk modulus, B_b	136.1	GPa	Adopted model input; bulk elastic data for CoCrFeMnNi; [36] and related elastic literature
Debye temperature, θ_{Db}	427	K	Reported/adopted CoCrFeMnNi alloy value; alloy value preferred to elemental averaging
Atomic packing factor, η	0.74	dimensionless	FCC packing factor
Anderson–Grüneisen parameter, δ	4	dimensionless	Adopted value used in the temperature-dependent thermal-expansion model; Kumar *et al.* [31]
Shape factor, α	1.00, 1.33, 0.67, 1.24, 1.18, 1.49	dimensionless	Table 1/Singh & Phantsi [25] for sphere, nanowire, nanofilm, hexahedron, octahedron, tetrahedron
Reference temperature, T_0	300	K	Room-temperature reference used in the thermal-expansion formulation
Bulk-model constant, k	4	dimensionless	Adopted in the size-dependent bulk-modulus model [32]

characteristic size varied over 5 - 55 nm in the size sweep. For nanofilms, h denotes the film thickness; h is the characteristic size varied over 5 - 55 nm, while the in-plane lateral dimensions are assumed sufficiently large compared with h so that the dominant finite-size contribution is associated with thickness. Because the six shapes do not share an identical mathematical dimension, the comparison is made at the same numerical characteristic size used by the adopted shape-specific equations; it is not an equal-volume comparison unless explicitly stated otherwise.

The atomic diameter d is taken as the effective atomic diameter associated with the FCC CoCrFeMnNi lattice. The bulk cohesive energy, melting temperature, bulk melting entropy, heat capacity, volumetric thermal expansion coefficient, bulk modulus, Debye temperature, atomic packing factor and Anderson–Grüneisen parameter are treated as bulk inputs to the corresponding nanosolid equations. Where the original model requires an alloy value, the equiatomic composition average is used; where a directly measured CoCrFeMnNi value is available, that alloy value is preferred. The numerical input values and their literature sources should therefore be read together with the equations below.

The calculations use an equiatomic CoCrFeMnNi alloy ($c_{Co} = c_{Cr} = c_{Fe} = c_{Mn} = c_{Ni} = 0.20$) and the FCC structure reported for the Cantor alloy. For any composition-averaged scalar property X, the equiatomic arithmetic average is used, $\bar{X} = \sum c_i X_i$. For properties for which direct experimental CoCrFeMnNi data are available, the measured alloy value is used preferentially rather than replacing it with an elemental average. This distinction is important because thermodynamic and elastic properties of concentrated solid solutions are not generally equal to simple elemental averages.

Numerical-input convention: The calculations use the following explicit bulk input at room temperature: $d = 0.254$ nm, E_{total}, $b \approx 386.7$ kJ mol^{-1}, $T_{mb} = 1607$ K, $S_{mb} \approx 8.3$ J mol^{-1} K^{-1}, $C_{pb} \approx 27.7$ J mol^{-1} K^{-1}, $\xi_b = 45 \times 10^{-6}$ K^{-1}, $B_b = 136.1$ GPa, $\theta_{Db} = 427$ K, $\eta = 0.74$, $\delta_T = 4$, $T_0 = 300$ K and $k = 4$. The shape factors are $\alpha = 1.00$, 1.33, 0.67, 1.24, 1.18 and 1.49 for spherical, nanowire, nanofilm, hexahedral, octahedral and tetrahedral geometries, respectively. Where a quantity is derived rather than independently measured, the derivation and source are stated in Table 1.

2.1. Surface Atom Fraction

The size-dependent behaviour of nanomaterials is strongly influenced by the fraction of atoms located at their surfaces. Surface atoms have lower coordination numbers and weaker effective interatomic bonding than atoms located in the interior of the nanomaterial. Consequently, the increasing surface-to-volume ratio at smaller dimensions produces significant deviations from the corresponding bulk properties. The surface atom fraction is therefore an important parameter for describing the size and shape dependence of nanomaterials [33] [37].

The surface atom fraction is defined as the ratio of the number of surface atoms to the total number of atoms in the nanostructure. It can be expressed in terms of the surface area and volume of the nanostructure as

$$\frac{N}{n} = \frac{\text{surface area of nanoparticle}/\text{surface area of an atom}}{\text{volume of nanoparticle}/\text{volume of an atom}} \tag{1}$$

where N is the number of surface atoms and n is the total number of atoms in the nanostructure.

For a spherical nanoparticle of diameter D, with d representing the atomic diameter, the surface-to-volume relation can be written as

$$\frac{N}{n} = \frac{4D^2}{d^2} \Big/ \frac{D^3}{d^3} = \frac{4d}{D} \tag{2}$$

The number of surface atoms depends not only on particle size but also on particle morphology, crystal structure and atomic packing. Therefore, a geometrical correction factor α is introduced to account for the effect of particle shape. The generalized expression for the surface atom fraction is given by

$$\frac{N}{n} = \frac{4\alpha d}{D} \tag{3}$$

Here, d is the atomic diameter, D is the characteristic dimension of the nanostruc-

ture and α is a dimensionless shape parameter that depends on the morphology of the nanostructure. The parameter N/n represents the fraction of atoms located at the surface and serves as the fundamental size-dependent parameter in the subsequent thermodynamic and thermoelastic calculations.

Table 2. N/n and Shape parameter for different nanosolids.

Nanosolids	N/n	N/2n	Shape parameter (α)
Spherical	4 d/D [23]	2 d/D	1.00 [25]
Nanowires	(8/3) d/l [23]	1.333 d/l	1.33 [25]
Nanofilm	(4/3) d/h [23]	0.665 d/h	0.67 [25]
Hexahedral	4 d/D [24]	2 d/D	1.24 [25]
Octahedral	(4.898) d/a [24]	2.449 d/a	1.18 [25]
Tetrahedral	(9.797) d/a [24]	4.898 d/a	1.49 [25]

2.2. Cohesive Energy

Cohesive energy is an important thermodynamic parameter for describing the strength of interatomic bonding and the stability of a material. In a nanostructure, the total cohesive energy is determined by contributions from both surface and interior atoms. Because surface atoms have reduced coordination numbers, their contribution to the total cohesive energy differs from that of atoms in the interior. Qi proposed a cohesive-energy model for nanosolids [26]. According to this model, the total cohesive energy of a nanostructure can be expressed as

$$E_{\text{total}} = E_0\left(n-N\right)+\frac{n}{2}E_n \tag{4}$$

Where, N stands for the number of surface atoms and n denotes the total number of atoms of nanosolids and E_0 represents cohesive energy per atom of the bulk material. $\left(n-N\right)$ is the number of interior atoms in the solid. The contribution of the interior atoms to the cohesive energy of the nanomaterials is therefore, $E_0\left(n-N\right)$.

Thus, the mathematical relation for cohesive energy E_n of nanomaterial as follows

$$E_n = \frac{AE_{\text{total}}}{n}$$

Where, A = Avogardo's number. Thus, the final expression for the cohesive energy of the nanomaterial E_n is given below and E_b represents the cohesive energy of bulk nanomaterial.

$$E_n = E_b\left(1-\frac{N}{2n}\right) \tag{5}$$

Qi and Wang proposed a model to give the cohesive energy of nanomaterials with $\frac{N}{n}$ for spherical nanosolids and bulk cohesive energy per atom (E_0) is given as

$$E_n = E_0\left(1-\frac{3N}{4n}\right) \tag{6}$$

For clarity, the comparison of F among morphologies is used only to describe the size- and shape-dependent thermodynamic response predicted by the adopted model. A statement that a morphology is "more stable" requires comparison with a defined reference state at identical T, V (or identical geometry/volume convention) and composition; therefore, higher numerical F is not by itself taken to mean greater thermodynamic stability.

Here, the cohesive-energy term is obtained from the surface-atom model described in Section 2.2; R is the gas constant; k_B is the Boltzmann constant; T is the temperature; θ_D is the size-dependent Debye temperature; and α is the dimensionless shape factor. The Debye function represents the vibrational contribution. All morphologies are evaluated using the same temperature and the same bulk-reference convention.

Thus, throughout Sections 2.3 and 3.2, the reported quantity is the Helmholtz free energy $F_{(T,V)}$, or its size-dependent change relative to the adopted bulk cohesive/vibrational reference. It is not interpreted as an absolute phase-stability criterion. At fixed T and composition, comparison among morphologies is meaningful only under the same geometry/volume convention and reference state; a higher numerical F does not by itself imply greater thermodynamic stability.

The present calculation is formulated in terms of the Helmholtz free energy, $F_{(T,V)}$, rather than the Gibbs free energy. This choice is consistent with the Debye-type vibrational formulation used here, in which volume is treated as the relevant geometrical variable and no independent pressure–volume term is evaluated. The calculated quantity therefore represents the Helmholtz free energy per mole of atoms relative to the same bulk reference convention used for the cohesive-energy term.

2.3. Helmholtz Free Energy (F)

The Helmholtz free energy of the CoCrFeMnNi nanostructures is evaluated by considering the cohesive-energy contribution (E_{cohesive}) together with the vibrational contribution (E_{vib}) described within the Debye model. The Helmholtz free energy is expressed as:

$$F_{(T,V)} = E_{\text{cohesive}} + E_{\text{vib}} = E_{\text{total}} + E_{\text{vib}} \tag{7}$$

where $F_{(T,V)}$ is the Helmholtz free energy at temperature (T) and volume (V), E_{cohesive} represents the static cohesive-energy contribution of the nanostructure, and E_{vib} denotes the vibrational Helmholtz free-energy contribution calculated using the Debye model. The vibrational contribution accounts for the thermal excitation of phonon modes and therefore incorporates the temperature dependence of the free energy. This formulation provides a thermodynamically consistent description of the temperature-dependent stability of the CoCrFeMnNi nanostructures.

2.4. Melting Entropy

The cohesive energy has been reported to exhibit a linear dependence on the melting temperature of materials. Based on this concept in mind, Qi has described the relation between the melting temperature [26] and Kumar *et al.* [28] has confirmed its feasibility by experimental studies.

$$\frac{T_{mn}}{T_{mb}} = 1 - \frac{N}{2n} \tag{8}$$

where T_{mn} and T_{mb} are the isolated nanostructure melting temperatures at the nanoscale level and the corresponding bulk material, respectively. $\frac{N}{2n}$ depends on the size and shape of the different nanostructures.

The corresponding melting temperature for the vibrational entropy S_{vib} of bulk crystal is given as: [28] [29]

$$S_{\text{vib}} = \frac{3R}{2} \ln\left(\frac{T_{mb}}{C}\right) \tag{9}$$

where C is a constant and R is the gas constant. The melting behaviour of metallic crystals has been found to be mostly vibrational. Therefore, the vibrational entropy is almost equal to the melting entropy for bulk crystals. Under this assumption, the bulk material is derived by a relation from Equation (9) as follows [30]:

$$S_{mb} = \frac{3R}{2} \ln\left(\frac{T_{mb}}{C}\right) \tag{10}$$

While the nanomaterials are defined as:

$$S_{mn} = \frac{3R}{2} \ln\left(\frac{T_{mn}}{C}\right) \tag{11}$$

On Combining Equation (10) and Equation (11), the following relation is obtained [28]:

$$S_{mn} = S_{mb} + \frac{3R}{2} \ln\left(\frac{T_{mn}}{T_{mb}}\right) \tag{12}$$

Where, S_{mn} and S_{mb} are the overall melting entropies of nanoparticles and their bulk material, respectively.

The thermodynamic parameter known as melting entropy indicates the degree of disorder generated when a solid transforms into a liquid [24]. This reform is influenced by the size and shape of the nanomaterials due to increases surface to volume ratio and decrease in cohesive energy. For nanomaterials, the decrease in melting entropy with decreasing particle size is attributed to the reduced vibrational component of overall melting entropy. Melting entropy is a critical parameter that reflects the thermodynamic reforms during the phase transition from solid to liquid and it is significantly affected by the size and shape of the nanomaterials is given by combining Equation (8) and Equation (12) as [24].

$$S_{mn} = S_{mb} + \frac{3R}{2} \ln\left(1 - \frac{N}{2n}\right) \tag{13}$$

Here, S_{mn} and S_{mb} are melting entropy of nanomaterials and their corresponding bulk materials respectively.

2.5. Specific Heat Capacity

The specific heat capacity is the amount of heat required to raise the temperature of a given quantity of a nanomaterial by one degree Celsius. Thus, the enhanced heat capacities are given as [37].

$$C_n = C_b\left(1-\frac{3N}{4n}\right)^{-1} \tag{14}$$

Here, C_n and C_b are specific heat capacity of nanomaterials and their corresponding bulk materials respectively.

2.6. Bulk Modulus and Thermal Expansivity

The relationship between the bulk modulus (B) and the volumetric thermal expansion coefficient (ξ) provides a fundamental basis for understanding size-dependent thermomechanical behaviour in nanostructured systems. Sharma *et al.* [31] developed a theoretical framework to describe the variation of volume thermal expansion in nanomaterials by incorporating atomic coordination effects.

According to this model, the volume thermal expansion coefficient of a nanomaterial (ξ_n) is related to that of its bulk counterpart (ξ_b) through the expression:

$$\xi_n = \xi_b\left(1-\frac{3N}{4n}\right)^{-1} \tag{15}$$

Here, ξ_n and ξ_b are the volumetric thermal expansion coefficients of the nanomaterial and bulk alloy, respectively. For equiatomic CoCrFeMnNi, the room-temperature linear thermal expansion coefficient is approximately 15×10^{-6} K^{-1}; under the isotropic approximation used in the present model, the corresponding volumetric coefficient is $\xi_b \approx 45 \times 10^{-6}$ K^{-1}. The value 136.1 GPa is not a thermal-expansion coefficient; it is a bulk-modulus value and is therefore used only in the elastic-property calculation. The thermal-expansion input is cited to the experimental CoCrFeMnNi study of Kumar *et al.* [33]. ξ_n and ξ_b for practical applications, the above relation can be reformulated in terms of geometrical parameters by expressing the surface-to-volume atomic ratio. For nanostructures of characteristic size D, the equation becomes:

$$\xi_n = \xi_b\left(1-\frac{2d}{\eta D}\right)^{-1} \tag{16}$$

Where, η represents the atomic packing factor and D is the Spherical Nanocrystal diameter. This expression highlights that thermal expansion is strongly size-dependent and increases as the particle size decreases.

Extending this model to anisotropic nanostructures, the geometry-specific forms Thus, expression for variation of volume thermal expansion for nanowire with nanowire diameter (L) is given as

$$\xi_n = \xi_b \left(1 - \frac{4d}{3L\eta}\right)^{-1} \tag{17}$$

Again, expression for variation of volume thermal expansion for nanofilm with nanofilm diameter (h) is given as

$$\xi_n = \xi_b \left(1 - \frac{2d}{3h\eta}\right)^{-1} \tag{18}$$

These expressions account for the dimensional confinement and altered surface atom fraction specific to one-dimensional (nanowires) and two-dimensional (nanofilms) systems.

Furthermore, Kumar *et al.* introduced a temperature-dependent modification to the thermal expansion behaviour of nanomaterials by incorporating the Anderson–Grüneisen parameter (δ_T), which quantifies the coupling between thermal expansion and elastic properties. According to this approach:

$$\frac{\xi_n}{\xi_b} = \left[1 - \xi_n \delta_T \left(T - T_0\right)\right]^{-1} \tag{19}$$

Where, T is the temperature and T_0 is a reference temperature (typically room temperature). The parameter δ_T characterizes the sensitivity of thermal expansion to temperature-induced changes in bulk modulus.

By substituting the size-dependent expression of ξ_n into the above relation, a combined size- and temperature-dependent model is obtained:

$$\frac{\xi_n}{\xi_b} = \left[1 - \xi_b \left(1 - \frac{3N}{4n}\right)^{-1} \delta_T \left(T - T_0\right)\right]^{-1} \tag{20}$$

This final expression captures the coupled influence of nanoscale size effects and thermal fluctuations on volumetric thermal expansion. It demonstrates that both reduced dimensions (through $\frac{N}{2n}$) and temperature elevation (through δ_T) contribute to the deviation of thermal expansion behaviour from bulk materials.

The expression for size and shape dependence of bulk modulus for different nanomaterials is given as [32] where $k = 4$ is dimensionless parameter and value of $\frac{N}{2n}$ is mentioned in **Table 2**.

$$B_n = B_b \left(1 - \frac{3N}{4n}\right)^k \tag{21}$$

Where B_n is the bulk modulus of the nanomaterials and B_b bulk modulus of the bulk materials.

3. Results and Discussion

3.1. Cohesive Energy

For the CoCrFeMnNi HEA alloy, cohesive energy increases with particle size across all configurations. At very small sizes (approximately 5 - 10 nm), the cohesive energy is significantly lower than the bulk value because a large fraction of

the atoms resides on the surface. Surface atoms have fewer nearest neighbours compared to atoms within the particle's interior, resulting in unsaturated bonds and overall weaker atomic binding. Consequently, nanoparticles exhibit lower cohesive energy than the corresponding bulk material.

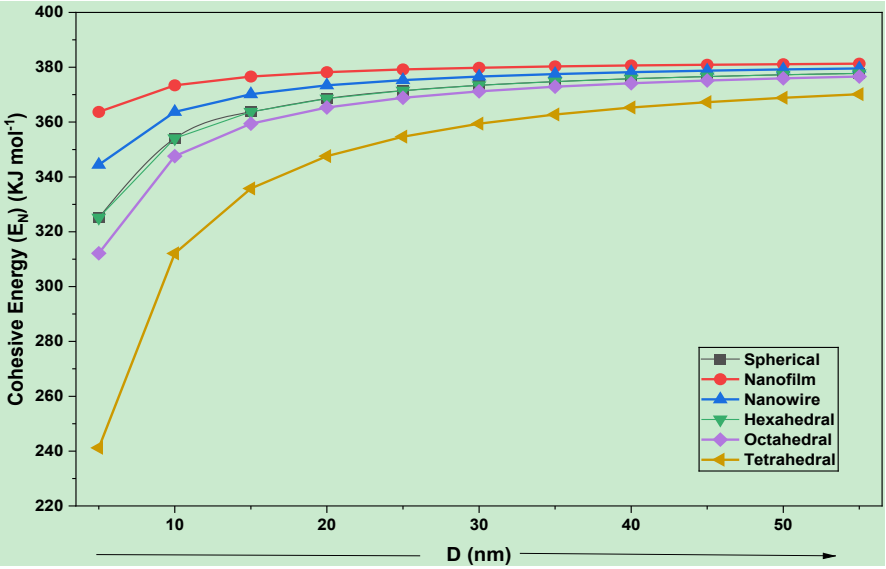

Figure 1. Shows the variations of cohesive energy with respect to size for different shapes of CoCrFeMnNi.

As shown in Figure 1 as the particle size increases from 5 nm to 55 nm, the proportion of surface atoms decreases. This leads to a gradual strengthening of the average bonding energy, causing the cohesive energy to rise rapidly at smaller sizes and more slowly at larger sizes. Beyond approximately 35 - 40 nm, the curves begin to converge, indicating that the influence of surface atoms becomes negligible and the nanoparticles start behaving like bulk material. This convergence demonstrates that the size effect is significant primarily within the nanoscale range. Among the geometries considered, the nanofilm exhibits the highest cohesive energy across the entire size range, reflecting a larger cohesive-energy value within the adopted surface-atom model; this difference is not, by itself, a thermodynamic response ranking. Spherical shapes retain relatively higher cohesive energy due to their lower surface-energy distribution. Nanowire, hexahedral and octahedral structures exhibit intermediate values, reflecting moderate surface atom fractions and coordination environments. In contrast, tetrahedral nanoparticles particularly at smaller sizes consistently display the lowest cohesive energy. As particle size increases, the surface contribution diminishes, thereby reducing the impact of particle size on total cohesive energy; notably, the differences between various shapes are most pronounced for very small nanoparticles and gradually decrease with increasing size, eventually converging toward a state equivalent to the thermodynamic limit of the bulk alloy.

3.2. Helmholtz Free Energy

Figure 2 illustrates the variation of the Helmholtz free energy (F) with nanoparticle

size for different morphologies of CoCrFeMnNi high-entropy alloy (HEA). The particle size ranges from approximately 5 to 55 nm, while the calculated F values vary from about 240 to 380 kJ mol^{-1}. A clear increase in F is observed with increasing particle size for all morphologies, with the most pronounced changes occurring in the smaller size range.

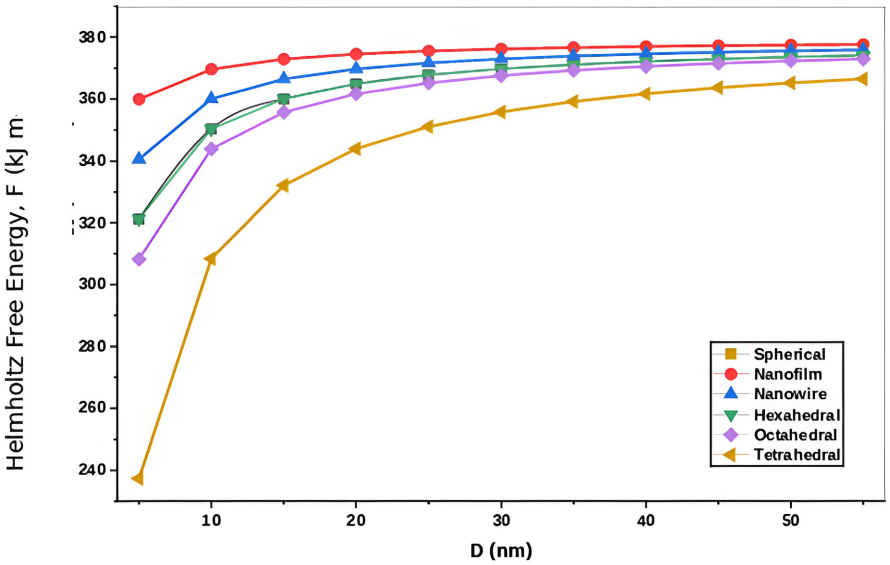

Figure 2. Variation of Helmholtz free energy (F) with characteristic size for different morphologies of CoCrFeMnNi HEA.

At the smallest size, the nanofilm exhibits the highest F (approximately 360 kJ mol^{-1}), whereas the tetrahedral morphology shows the lowest F (approximately 240 kJ mol^{-1}). The other morphologies—spherical, nanowire, hexahedral and octahedral—show intermediate values. Thus, the difference between the highest and lowest F is approximately 120 kJ mol^{-1}, demonstrating a strong morphology-dependent thermodynamic response at smaller sizes. These values are compared within the same Helmholtz-free-energy formulation and reference convention; the numerical ordering is not interpreted as a ranking of absolute thermodynamic response.

With increasing size, F increases rapidly up to approximately 20 - 30 nm, after which the rate of increase gradually decreases. Beyond approximately 35 - 40 nm, the curves become relatively flatter and progressively converge, reaching approximately 370 - 380 kJ mol^{-1} at 50 - 55 nm. This convergence indicates that the influence of morphology becomes less pronounced at larger particle sizes. The observed trend can be attributed to the decreasing surface-to-volume ratio and surface-atom fraction with increasing nanoparticle size, which reduces the relative contribution of surface effects to the overall Helmholtz free energy.

The values of F are evaluated at the same temperature and composition, with the size-dependent nanosolid result compared within the same Helmholtz-free-energy formulation. They should therefore be interpreted as model-calculated free-energy values relative to the adopted cohesive/vibrational reference, not as absolute phase-stability rankings. In particular, a higher F does not imply greater

thermodynamic response.

Overall, Figure 2 demonstrates that Helmholtz free energy is strongly dependent on both nanoparticle size and morphology, particularly in the smaller nanoscale regime. The progressive convergence of the curves at larger sizes suggests a transition from a strongly surface- and morphology-dependent regime toward a more bulk-like thermodynamic behaviour.

3.3. Melting Entropy

For all nanoparticle geometries, melting entropy consistently increases as particle size increases(Figure 3). This increase is most pronounced in the smaller size range (approximately 5 - 20 nm); however, as the particle size exceeds roughly 35 - 40 nm, the rate of increase gradually diminishes, with the curves for different geometries converging toward similar values. This behaviour demonstrates that nanoscale surface effects are most significant at very small particle sizes and gradually subside as the particles grow larger. The reduction in melting entropy observed in small nanoparticles is primarily attributed to the higher proportion of surface atoms. Compared to atoms within the particle's interior, surface atoms have fewer nearest neighbors, resulting in lower atomic coordination and weaker interatomic bonding. These unsaturated surface bonds render the atomic arrangement less stable and cause thermodynamic properties to deviate from those of the bulk material. As particle size increases, the proportion of interior atoms rises while the fraction of surface atoms decreases. Consequently, the atomic structure increasingly resembles that of the bulk alloy, leading to a gradual rise in melting entropy towards the bulk value.

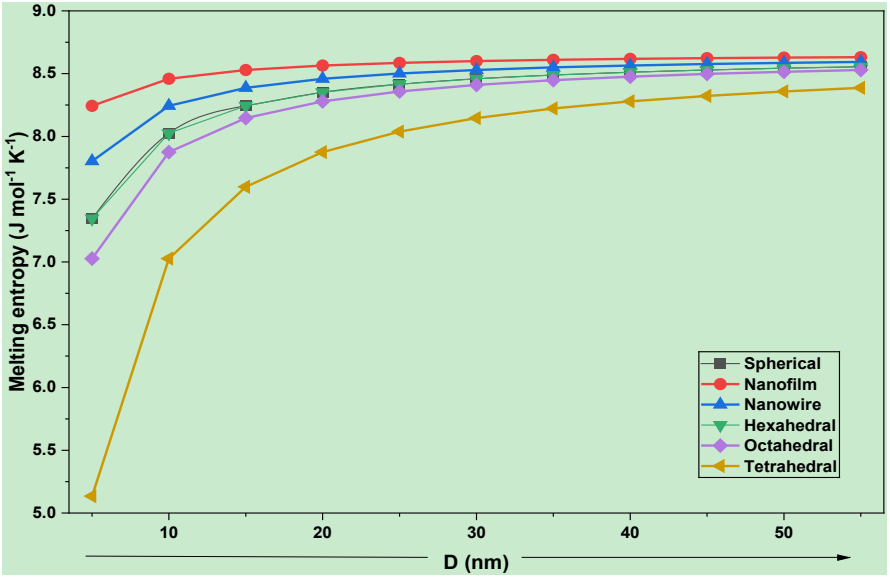

Figure 3. Shows the variations of Melting entropy with respect to sizes (*D*) for different shapes of CoCrFeMnNi HEA alloys.

Among the geometries considered, the nanofilm exhibits the highest melting entropy within the examined size range, indicating that its thermodynamic behaviour approaches the bulk state more rapidly than that of other geometries. Spherical and

nanowire nanoparticles also show relatively higher melting entropy, followed by hexahedral and octahedral structures. In contrast, tetrahedral nanoparticles consistently display the lowest melting entropy, particularly at very small particle sizes. This behaviour can be attributed to the comparatively large proportion of edge and corner atoms; these atoms possess the lowest coordination numbers and thus contribute more significantly to surface-related thermodynamic effects. As a result, tetrahedral nanoparticles experience the greatest reduction in melting entropy. Another significant observation is that the differences between the various geometries are substantial at small particle sizes where the surface atom fraction is large and highly dependent on particle dimensions but as the particle size increases to approximately 55 nm, the curves converge toward a common value. This convergence indicates that shape-dependent surface effects gradually diminish and thermodynamic behaviour becomes governed primarily by the bulk atomic structure rather than the external geometry. Controlling both particle size and geometry offers an effective strategy for tuning the thermal stability of CoCrFeMnNi high-entropy alloy nanoparticles.

3.4. Specific Heat Capacity

Figure 4 shows that the normalized specific heat capacity decreases steadily with increasing particle size for all nanoparticle geometries. This decrease is particularly pronounced in the small particle-size range (approximately 5 - 15 nm), after which the curve gradually flattens and approaches the bulk value as particle size increases beyond approximately 35 - 40 nm. This trend indicates that nanoscale particles have significantly higher heat-storage capabilities than their bulk counterparts, while larger nanoparticles gradually regain bulk-like thermal behaviour.

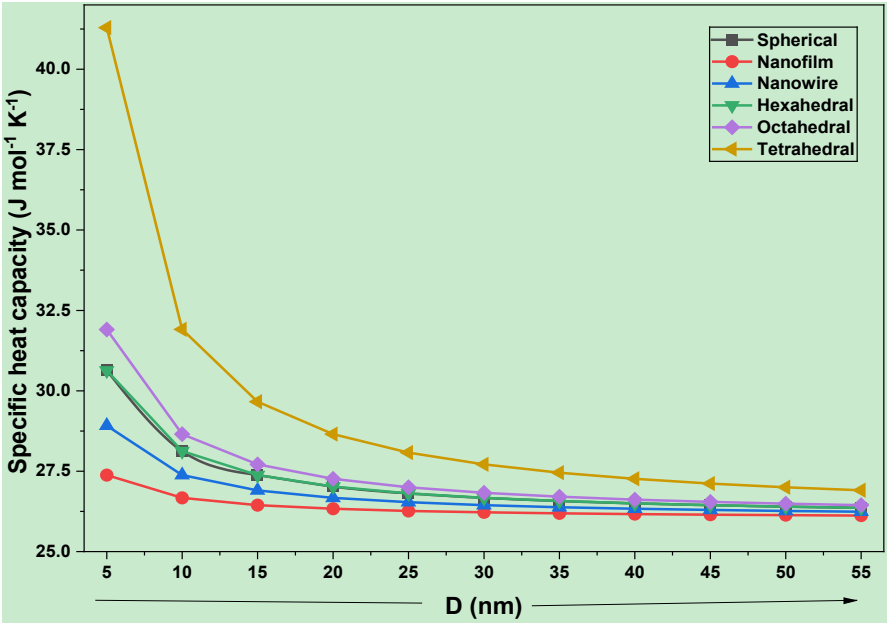

Figure 4. Shows the variations of specific heat capacity with respect to sizes (*D*) for different shapes of CoCrFeMnNi HEA alloys.

The increase in specific heat capacity at very small particle sizes is due to the dominance of surface atoms. Surface atoms have lower coordination numbers and weaker interatomic bonding than the atoms within the particle. Because these atoms are less tightly bound, they can perform more vibrational motion and absorb thermal energy more easily. Consequently, raising the nanoparticle's temperature requires more thermal energy, increasing the specific heat capacity. As particle size increases, the contribution of surface atoms decreases while that of tightly bound internal atoms increases. This reduces the contribution of surface vibrational modes and the specific heat capacity gradually decreases toward the bulk value. Particle geometry also significantly influences thermal behaviour. Of all geometries, tetrahedral nanoparticles exhibit the highest normalized specific heat capacity across the size range examined, especially at particle sizes less than 10 nm. This is because tetrahedral particles have the largest proportion of edge and corner atoms, resulting in the highest proportion of under-coordinated surface atoms. These atoms contribute strongly to lattice vibrations and increase the thermal energy storage capacity. Octahedral, hexahedral and nanowire geometries exhibit intermediate values, reflecting the moderate proportion of surface atoms. In contrast, spherical and nanofilm nanoparticles exhibit the lowest normalized specific heat capacities because their atomic arrangements have comparatively fewer under-coordinated surface atoms and stronger average interatomic bonding. Surface effects dominate thermophysical behaviour only in the nanoscale regime, while for larger particles, the influence of particle geometry becomes negligible as the surface-to-volume ratio becomes significantly lower. Eventually, the specific heat capacity approaches the bulk value, indicating that the thermodynamic behaviour is primarily controlled by the internal atoms.

The observed behaviour is consistent with theoretical size-dependent thermodynamic models, in which the increase in specific heat capacity is due to the increased contribution of surface atoms to lattice vibrations. As particle size decreases, the surface atom fraction (N/n) increases, leading to greater surface vibrational effects and energy absorption. Conversely, with increasing particle size, the surface contribution decreases and gradually returns to bulk thermodynamic behaviour. The excellent agreement between the theoretical trend and the calculated results confirms the validity of the size-dependent model for describing the thermal properties of CoCrFeMnNi nanoparticles.

3.5. Thermal Expansion

Figure 5 presents the variation of the volume thermal expansion coefficient, ξ_N, with particle size for the six different morphologies of CoCrFeMnNi HEA. A clear decrease in the thermal expansion coefficient is observed with increasing particle size for all the investigated nanostructures. The decrease is particularly pronounced in the smaller size range, whereas the rate of variation becomes progressively smaller at larger particle sizes. This behaviour indicates that the thermal expansion response is strongly influenced by nanoscale surface effects, which be-

come less significant as the particle size increases. The observed trend is consistent with the size-dependent theoretical formulation used in the present study, according to which the thermal expansion coefficient increases with decreasing particle size.

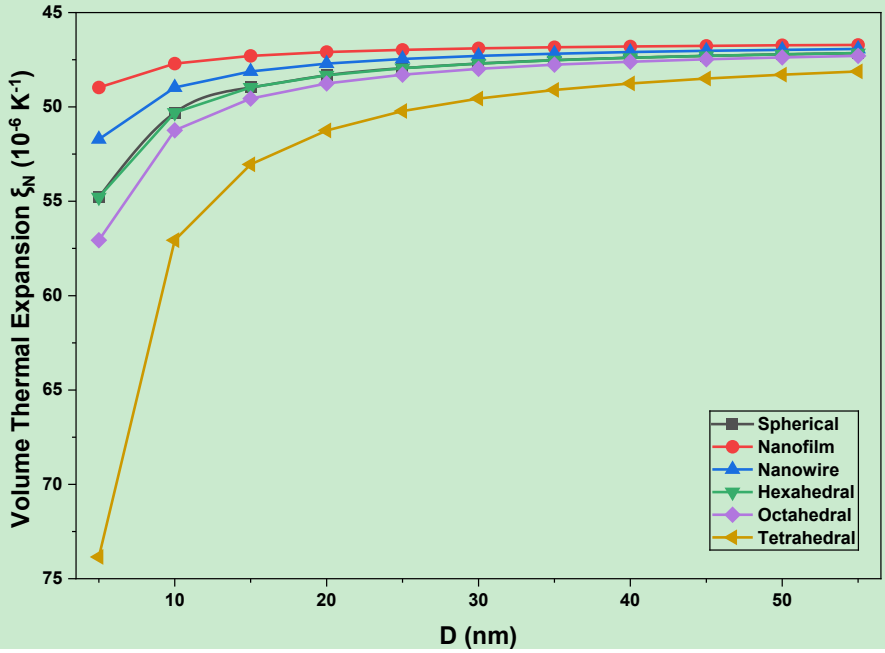

Figure 5. Variation of the volumetric thermal expansion coefficient (ξ_n) with characteristic size for different morphologies of CoCrFeMnNi HEA.

Among the different morphologies, the tetrahedral nanoparticles exhibit the highest thermal expansion coefficient at the smallest particle size, followed by the nanofilm and spherical structures, whereas the nanowire, hexahedral and octahedral structures show comparatively lower values in the initial size range. The particularly high value for the tetrahedral morphology can be associated with its larger effective surface-atom fraction and greater contribution from under-coordinated atoms. Such surface atoms possess altered bonding environments and enhanced anharmonic lattice vibrations, which contribute to the higher thermal expansion at very small dimensions.

With increasing particle size, the thermal expansion coefficient decreases for all morphologies and the differences between the curves gradually become smaller. The most significant morphology-dependent differences are therefore observed in the low-size regime, where the surface-to-volume ratio and the fraction of surface atoms are relatively high. At larger particle sizes, the curves approach one another, indicating a progressive reduction in the influence of morphology and a transition towards bulk-like thermal behaviour. This convergence is consistent with the general surface-atom-based interpretation adopted throughout the study, in which the contribution of surface atoms decreases as the characteristic dimension increases.

Overall, Figure 5 demonstrates that both particle size and morphology strongly

influence the thermal expansion behaviour of CoCrFeMnNi HEA nanostructures, with the effect being most pronounced at smaller particle sizes. The enhanced thermal expansion at reduced dimensions and its gradual decrease towards the bulk regime can be attributed primarily to the decreasing surface-atom fraction and the corresponding reduction in surface-induced lattice anharmonicity.

3.6. Bulk Modulus

Figure 6 illustrates the variation of bulk modulus with particle size for the six different morphologies of CoCrFeMnNi HEA. The bulk modulus increases systematically with increasing particle size for all the investigated nanostructures. The increase is particularly pronounced at smaller particle sizes, whereas the rate of increase gradually decreases with increasing size. This behaviour indicates a strong size dependence of the elastic response in the nanoscale regime, where the high fraction of surface atoms significantly influences the resistance of the nanostructures to volumetric deformation.

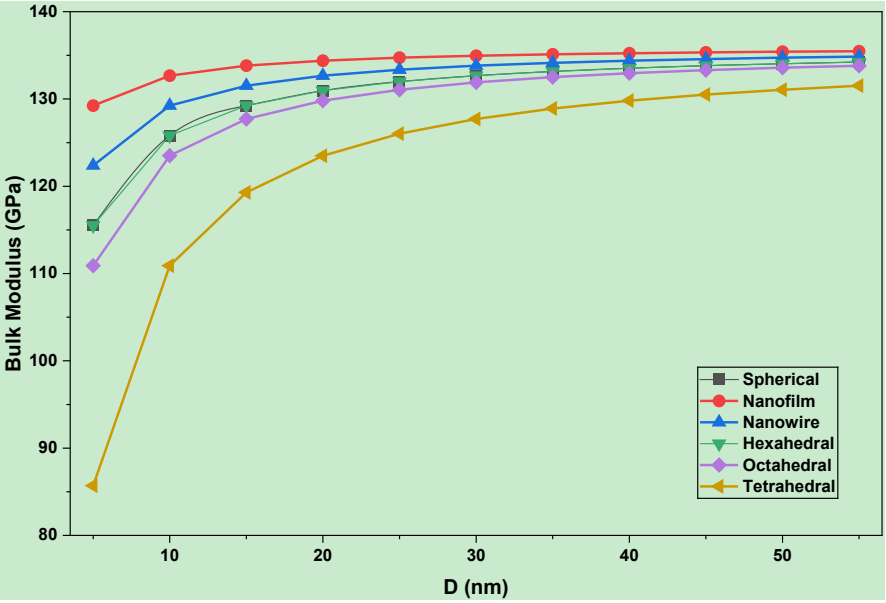

Figure 6. Shows the variations of bulk modulus with respect to sizes (D) for different shapes of CoCrFeMnNi HEA alloys.

At the smallest investigated size, the nanofilm exhibits the highest bulk modulus, with a value of approximately 130 GPa, followed by the spherical and nanowire structures. The hexahedral and octahedral morphologies show comparatively lower values, while the tetrahedral nanoparticle exhibits the lowest bulk modulus, approximately 86 GPa. Thus, a pronounced morphology-dependent difference is observed at the smallest particle size. The particularly low bulk modulus of the tetrahedral structure can be attributed to its relatively high surface-atom fraction and greater contribution of under-coordinated atoms, which results in stronger surface relaxation and weaker resistance to compression.

With increasing particle size, the bulk modulus of all morphologies increases

progressively. The tetrahedral structure shows the most pronounced increase, rising from approximately 86 GPa at 5 nm to around 131 GPa at 55 nm. The other morphologies exhibit comparatively smaller changes because their initial bulk-modulus values are already closer to the bulk limit. As the particle size increases, the differences among the different geometries become progressively smaller, demonstrating that the influence of morphology is strongest at small dimensions.

Beyond approximately 30 - 40 nm, the curves become relatively flat and approach closely spaced values in the range of approximately 133 - 135 GPa. These values are close to the reported bulk modulus of the corresponding bulk material, indicating a gradual transition from surface-dominated nanoscale behaviour towards bulk-like elastic behaviour. The convergence of the curves further suggests that the contribution of surface atoms and geometrical effects becomes progressively less significant as the particle size increases.

Overall, **Figure 6** demonstrates that bulk modulus is strongly dependent on both particle size and morphology, particularly in the small-size regime. The pronounced reduction in bulk modulus at smaller dimensions, especially for the tetrahedral morphology, reflects the dominant role of surface atoms and reduced atomic coordination. With increasing particle size, the progressive recovery of bulk modulus and convergence of the different curves indicate diminishing surface effects and an approach towards the bulk elastic limit.

4. Conclusions

The present theoretical investigation provides a systematic understanding of the size- and morphology-dependent thermophysical and thermoelastic behaviour of CoCrFeMnNi high-entropy alloy nanostructures. Six different morphologies—spherical, tetrahedral, hexahedral, octahedral, nanowire and nanofilm—were investigated over the size range of 5 - 55 nm using a unified size- and shape-dependent theoretical framework.

The results demonstrate that particle size and morphology strongly influence the cohesive energy, Helmholtz free energy, melting entropy, specific heat capacity, thermal expansion coefficient and bulk modulus, particularly in the small-size regime. These variations are primarily associated with the increasing contribution of surface atoms, reduced atomic coordination, surface relaxation and morphology-dependent atomic packing. Among the investigated structures, tetrahedral nanostructures exhibit the strongest size dependence, reflecting their relatively high effective surface-atom fraction and pronounced contribution of under-coordinated atoms. Consequently, they generally exhibit lower cohesive energy, melting entropy and bulk modulus, together with enhanced thermal expansion and specific heat capacity at smaller dimensions.

The thermodynamic and thermoelastic responses also show a clear morphology-dependent hierarchy at small particle sizes. Nanofilms exhibit particularly high cohesive-energy and Helmholtz-free-energy values within the adopted model, whereas tetrahedral structures generally represent the most surface-sensi-

tive morphology. These numerical differences describe the morphology-dependent response predicted by the model and are not, by themselves, interpreted as absolute thermodynamic-stability rankings without a common reference state.

With increasing particle size, the differences among the six morphologies progressively decrease. For most investigated properties, the curves approach closely spaced values beyond approximately 35 - 50 nm, indicating a gradual transition from surface-dominated nanoscale behaviour towards bulk-like behaviour. This convergence demonstrates that the relative contribution of surface atoms diminishes with increasing size, while the internal atomic network increasingly governs the overall material response.

Overall, the study establishes that particle size and morphology are effective parameters for tailoring the thermophysical and thermoelastic characteristics of CoCrFeMnNi HEA nanostructures. The unified correlations obtained among surface-atom fraction, atomic coordination, thermodynamic response, thermal response and elastic behaviour provide useful theoretical insight into the design of morphology-controlled CoCrFeMnNi nanostructures for advanced thermal, mechanical and nanoscale engineering applications.

Author Contributions

Conceptualisation: Jagdhar Mandal; Methodology: Pinki Kumari; Analysis: Sonal Swaraj & Nirjar Vrind; Writing, Review and Editing: Krishna Kumar & Mritunjay Kumar; Investigation: Pinky Kumari, Sonal Swaraj & Nirjar Vrind; Validation & Supervision: Jagdhar Mandal.

Conflicts of Interest

Authors declare no conflict of interest for the publication of paper.

References

[1] Laplanche, G., Gadaud, P., Horst, O., Otto, F., Eggeler, G. and George, E.P. (2015) Temperature Dependencies of the Elastic Moduli and Thermal Expansion Coefficient of an Equiatomic, Single-Phase CoCrFeMnNi High-Entropy Alloy. *Journal of Alloys and Compounds*, **623**, 348-353. https://doi.org/10.1016/j.jallcom.2014.11.061

[2] Cantor, B., Chang, I.T.H., Knight, P. and Vincent, A.J.B. (2004) Microstructural Development in Equiatomic Multicomponent Alloys. *Materials Science and Engineering*: *A*, **375**, 213-218. https://doi.org/10.1016/j.msea.2003.10.257

[3] Otto, F., Yang, Y., Bei, H. and George, E.P. (2013) Relative Effects of Enthalpy and Entropy on the Phase Stability of Equiatomic High-Entropy Alloys. *Acta Materialia*, **61**, 2628-2638. https://doi.org/10.1016/j.actamat.2013.01.042

[4] Senkov, O.N., Wilks, G.B., Scott, J.M. and Miracle, D.B. (2011) Mechanical Properties of $Nb_{25}Mo_{25}Ta_{25}W_{25}$ and $V_{20}Nb_{20}Mo_{20}Ta_{20}W_{20}$ Refractory High Entropy Alloys. *Intermetallics*, **19**, 698-706. https://doi.org/10.1016/j.intermet.2011.01.004

[5] Senkov, O.N., Scott, J.M., Senkova, S.V., Meisenkothen, F., Miracle, D.B. and Woodward, C.F. (2012) Microstructure and Elevated Temperature Properties of a Refractory TaNbHfZrTi Alloy. *Journal of Materials Science*, **47**, 4062-4074. https://doi.org/10.1007/s10853-012-6260-2

[6] Zou, Y., Maiti, S., Steurer, W. and Spolenak, R. (2014) Size-Dependent Plasticity in an $Nb_{25}Mo_{25}Ta_{25}W_{25}$ Refractory High-Entropy Alloy. *Acta Materialia*, **65**, 85-97. https://doi.org/10.1016/j.actamat.2013.11.049

[7] Wu, Y.S., Xu, C.M., Guo, J.X., Su, Q.M., Du, G.H. and Zhang, J. (2014) Enhanced Electrochemical Performance by Wrapping Graphene on Carbon Nanotube/Sulfur Composites for Rechargeable Lithium-Sulfur Batteries. *Materials Letters*, **137**, 277-280. https://doi.org/10.1016/j.matlet.2014.09.044

[8] Couzinié, J.P., Dirras, G., Perrière, L., Chauveau, T., Leroy, E., Champion, Y., *et al.* (2014) Microstructure of a Near-Equimolar Refractory High-Entropy Alloy. *Materials Letters*, **126**, 285-287. https://doi.org/10.1016/j.matlet.2014.04.062

[9] Lilensten, L., Couzinié, J.P., Perrière, L., Bourgon, J., Emery, N. and Guillot, I. (2014) New Structure in Refractory High-Entropy Alloys. *Materials Letters*, **132**, 123-125. https://doi.org/10.1016/j.matlet.2014.06.064

[10] Yao, M.J., Pradeep, K.G., Tasan, C.C. and Raabe, D. (2014) A Novel, Single Phase, Non-Equiatomic FeMnNiCoCr High-Entropy Alloy with Exceptional Phase Stability and Tensile Ductility. *Scripta Materialia*, **72**, 5-8. https://doi.org/10.1016/j.scriptamat.2013.09.030

[11] He, J.Y., Liu, W.H., Wang, H., Wu, Y., Liu, X.J., Nieh, T.G., *et al.* (2014) Effects of Al Addition on Structural Evolution and Tensile Properties of the FeCoNiCrMn High-Entropy Alloy System. *Acta Materialia*, **62**, 105-113. https://doi.org/10.1016/j.actamat.2013.09.037

[12] Liu, W., Tu, H.L., Gao, M., Su, X.P., Zhang, S.Y., Huo, C.S., *et al.* (2013) High Performance DLC/BP and ZnS/YbF_3 Double-Layer Protective and Antireflective Coatings. *Journal of Alloys and Compounds*, **581**, 526-529. https://doi.org/10.1016/j.jallcom.2013.07.130

[13] Bhattacharjee, P.P., Sathiaraj, G.D., Zaid, M., Gatti, J.R., Lee, C., Tsai, C., *et al.* (2014) Microstructure and Texture Evolution during Annealing of Equiatomic CoCrFeMnNi High-Entropy Alloy. *Journal of Alloys and Compounds*, **587**, 544-552. https://doi.org/10.1016/j.jallcom.2013.10.237

[14] Wu, Z., Bei, H., Otto, F., Pharr, G.M. and George, E.P. (2014) Recovery, Recrystallization, Grain Growth and Phase Stability of a Family of FCC-Structured Multi-Component Equiatomic Solid Solution Alloys. *Intermetallics*, **46**, 131-140. https://doi.org/10.1016/j.intermet.2013.10.024

[15] Otto, F., Hanold, N.L. and George, E.P. (2014) Microstructural Evolution after Thermomechanical Processing in an Equiatomic, Single-Phase CoCrFeMnNi High-Entropy Alloy with Special Focus on Twin Boundaries. *Intermetallics*, **54**, 39-48. https://doi.org/10.1016/j.intermet.2014.05.014

[16] Bykov, V., Kulikova, T., Sipatov, I., Sterkhov, E., Ko-valenko, D. and Ryltsev, R. (2023) Transport Properties of Equiatomic CoCrFeNi High-Entropy Alloy with a Single-Phase Face-Centered Cubic Structure. https://doi.org/10.20944/preprints202310.0832.v1

[17] Guo, W., Su, J., Lu, W., Liebscher, C.H., Kirchlechner, C., Ikeda, Y., *et al.* (2020) Dislocation-Induced Breakthrough of Strength and Ductility Trade-Off in a Non-Equiatomic High-Entropy Alloy. *Acta Materialia*, **185**, 45-54. https://doi.org/10.1016/j.actamat.2019.11.055

[18] Xin, Y., Li, S., Qian, Y., Zhu, W., Yuan, H., Jiang, P., *et al.* (2020) High-Entropy Alloys as a Platform for Catalysis: Progress, Challenges, and Opportunities. *ACS Catalysis*, **10**, 11280-11306. https://doi.org/10.1021/acscatal.0c03617

[19] Amiri, A. and Shahbazian-Yassar, R. (2021) Recent Progress of High-Entropy Mate-

rials for Energy Storage and Conversion. *Journal of Materials Chemistry A*, **9**, 782-823. https://doi.org/10.1039/d0ta09578h

[20] Jin, K., Sales, B.C., Stocks, G.M., Samolyuk, G.D., Daene, M., Weber, W.J., *et al.* (2016) Tailoring the Physical Properties of Ni-Based Single-Phase Equiatomic Alloys by Modifying the Chemical Complexity. *Scientific Reports*, **6**, Article No. 20159. https://doi.org/10.1038/srep20159

[21] Jin, K., Mu, S., An, K., Porter, W.D., Samolyuk, G.D., Stocks, G.M., *et al.* (2017) Thermophysical Properties of Ni-Containing Single-Phase Concentrated Solid Solution Alloys. *Materials & Design*, **117**, 185-192. https://doi.org/10.1016/j.matdes.2016.12.079

[22] Chou, H., Chang, Y., Chen, S. and Yeh, J. (2009) Microstructure, Thermophysical and Electrical Properties in $Al_xCoCrFeNi$ ($0 \le x \le 2$) High-Entropy Alloys. *Materials Science and Engineering: B*, **163**, 184-189. https://doi.org/10.1016/j.mseb.2009.05.024

[23] Shahmir, H., Mehranpour, M.S., Arsalan Shams, S.A. and Langdon, T.G. (2023) Twenty Years of the CoCrFeNiMn High-Entropy Alloy: Achieving Exceptional Mechanical Properties through Microstructure Engineering. *Journal of Materials Research and Technology*, **23**, 3362-3423. https://doi.org/10.1016/j.jmrt.2023.01.181

[24] Sharma, S. and Singh, J.P. (2024) Development of Size and Shape Dependent Model for Various Thermodynamic Properties of Nanomaterials. *Physics Open*, **19**, Article ID: 100215. https://doi.org/10.1016/j.physo.2024.100215

[25] Singh, M. and Phantsi, T.D. (2018) Bond Theory Model to Study Cohesive Energy, Thermal Expansion Coefficient and Specific Heat of Nanosolids. *Chinese Journal of Physics*, **56**, 2948-2957. https://doi.org/10.1016/j.cjph.2018.09.029

[26] Qi, W.H. (2005) Size Effect on Melting Temperature of Nanosolids. *Physica B: Condensed Matter*, **368**, 46-50. https://doi.org/10.1016/j.physb.2005.06.035

[27] Xiong, S., Qi, W., Huang, B., Wang, M. and Li, Y. (2010) Size and Shape Dependent Gibbs Free Energy and Phase Stability of Titanium and Zirconium Nanoparticles. *Materials Chemistry and Physics*, **120**, 446-451. https://doi.org/10.1016/j.matchemphys.2009.11.043

[28] Kumar, R., Sharma, G. and Kumar, M. (2013) Effect of Size and Shape on the Vibrational and Thermodynamic Properties of Nanomaterials. *Journal of Thermodynamics*, **2013**, Article ID: 328051. https://doi.org/10.1155/2013/328051

[29] Ubbelohde, A.R. (1965) Melting and Crystal Structure. Clarendon Press, 312-314.

[30] Xiong, S., Qi, W., Cheng, Y., Huang, B., Wang, M. and Li, Y. (2011) Universal Relation for Size Dependent Thermodynamic Properties of Metallic Nanoparticles. *Physical Chemistry Chemical Physics*, **13**, 10652. https://doi.org/10.1039/c0cp90161j

[31] Kumar, R., Sharma, G. and Kumar, M. (2013) Size and Temperature Effect on Thermal Expansion Coefficient and Lattice Parameter of Nanomaterials. *Modern Physics Letters B*, **27**, Article ID: 1350180. https://doi.org/10.1142/s0217984913501807

[32] Pandey, V. and Kumar, M. (2022) Development of Size and Shape Dependent Model for Bulk Modulus from Bulk to Nanoscale. *Physica B: Condensed Matter*, **629**, Article ID: 413617. https://doi.org/10.1016/j.physb.2021.413617

[33] Kumar, M., Kumar, K., Kumar, S., Kumari, N. andMandal, J. (2025) A Theoretical Investigation of Shape and Size Dependent Band Gap of (CdxZn1-x)Se Semiconductor Nanomaterial. *International Journal of Current Science* (*IJCSPUB*), **15**, 722-731. http://doi.one/10.1729/Journal.43792

[34] Reis, H.A., Elri, K.G., Sezer, R., Polat, G. and Öztürk, B. (2026) Investigating the Role

of Nickel in CoCrFeMnNi$_x$ High-Entropy Alloys: Thermodynamic Analysis and Molecular Dynamics Simulations. *Modelling and Simulation in Materials Science and Engineering*, **34**, Article ID: 065001. https://doi.org/10.1088/1361-651x/ae8d43

[35] Vaidya, M., Pradeep, K.G., Murty, B.S., Wilde, G. and Divinski, S.V. (2018) Bulk Tracer Diffusion in CoCrFeNi and CoCrFeMnNi High Entropy Alloys. *Acta Materialia*, **146**, 211-224. https://doi.org/10.1016/j.actamat.2017.12.052

[36] Yu, P.F., Zhang, L.J., Cheng, H., Zhang, H., Ma, M.Z., Li, Y.C., *et al.* (2016) The High-Entropy Alloys with High Hardness and Soft Magnetic Property Prepared by Mechanical Alloying and High-Pressure Sintering. *Intermetallics*, **70**, 82-87. https://doi.org/10.1016/j.intermet.2015.11.005

[37] Kumar, K., Kumar, M., Ahmad, S., Kumar, A. and Mandal, J. (2025) A Study of Shape and Size Dependent Thermodynamic Properties of Cu_xAl_{1-X} Nanomaterials. *International Journal of Physics and Applications*, **7**, 58-65. https://doi.org/10.33545/26647575.2025.v7.i1a.128

[38] Li, H., Huang, Y., Sun, J. and Lu, Y. (2021) The Relationship between Thermo-Mechanical History, Microstructure and Mechanical Properties in Additively Manufactured CoCrFeMnNi High Entropy Alloy. *Journal of Materials Science & Technology*, **77**, 187-195. https://doi.org/10.1016/j.jmst.2020.10.052

[39] Gelisio, L., Beyerlein, K.R. and Scardi, P. (2013) Atomistic Modeling of Lattice Relaxation in Metallic Nanocrystals. *Thin Solid Films*, **530**, 35-39. https://doi.org/10.1016/j.tsf.2012.07.063